Unraveling the Substrate−Metal Binding Site of Ferrochelatase: An X-ray Absorption Spectroscopic Study†

Gloria C. Ferreira,*,‡ Ricardo Franco,‡,§ Arianna Mangravita,‡ and Graham N. George*,⊥

Department of Biochemistry and Molecular Biology, College of Medicine, Institute for Biomolecular Science and H. Lee Moffitt Cancer Center and Research Institute, University of South Florida, Tampa, Florida 33612, and Stanford Synchrotron Radiation Laboratory, Stanford Linear Accelerator Center, MS 69, 2575 Sand Hill Road, Menlo Park, California 94205

Received September 27, 2001; Revised Manuscript Received January 6, 2002

ABSTRACT: Ferrochelatase (EC 4.99.1.1), the terminal enzyme of the heme biosynthetic pathway, catalyzes the insertion of ferrous iron into the protoporphyrin IX ring. Ferrochelatases can be arbitrarily divided into two broad categories: those with and those without a [2Fe-2S] center. In this work we have used X-ray absorption spectroscopy to investigate the metal ion binding sites of murine and *Saccharomyces cerevisiae* (yeast) ferrochelatases, which are representatives of the former and latter categories, respectively. Co^{2+} and Zn^{2+} complexes of both enzymes were studied, but the Fe^{2+} complex was only studied for yeast ferrochelatase because the [2Fe-2S] center of the murine enzyme interferes with the analysis. Co^{2+} and Zn^{2+} binding to site-directed mutants of the murine enzyme were also studied, in which the highly conserved and potentially metal-coordinating residues H207 and Y220 were substituted by residues that should not coordinate metal (i.e., H207N, H207A, and Y220F). Our experiments indicate four-coordinate zinc with $Zn(N/O)_3(S/Cl)_1$ coordination for the yeast and $Zn(N/O)_2(S/Cl)_2$ coordination for the wild-type murine enzyme. In contrast to zinc, a six-coordinate site for Co^{2+} coordinated with oxygen or nitrogen was present in both the yeast and murine (wild-type and mutated) enzymes, with evidence of two histidine ligands in both. Like Co^{2+}, Fe^{2+} bound to yeast ferrochelatase was coordinated by approximately six oxygen or nitrogen ligands, again with evidence of two histidine ligands. For the murine enzyme, mutation of both H207 and Y220 significantly changed the spectra, indicating a likely role for these residues in metal ion substrate binding. This is in marked disagreement with the conclusions from X-ray crystallographic studies of the human enzyme, and possible reasons for this are discussed.

Ferrochelatase (protoheme ferrolyase, EC 4.99.1.1) is the terminal enzyme of the heme biosynthetic pathway. It catalyzes the insertion of ferrous iron into protoporphyrin IX (*1*−*3*). In vitro, the enzyme exhibits a fairly wide substrate specificity. It is capable of utilizing several other divalent transition metal ions such as Co^{2+} and Zn^{2+} and a wide variety of IX isomer porphyrins (*1*); Fe^{3+}, however, is not a substrate (*4*). All animal ferrochelatases identified to date appear to contain a [2Fe-2S] cluster (*5*−*7*), and until recently it was believed that ferrochelatases from bacteria, yeast, algae, and higher plants lacked this site. However, the recent finding of such clusters in ferrochelatases from the fission yeast *Schizosaccaromyces pombe* and from a few bacteria (*3*) invalidates this generalization. Nevertheless, the enzymes are often arbitrarily divided into two categories: those with and those without the iron−sulfur cluster.

The ferrochelatase kinetic reaction mechanism has been proposed to be an ordered bi-bi sequential mechanism, in which iron binding occurs prior to that of porphyrin (*8*, *9*), and a random bi-bi mechanism, with either of the two substrates initially binding without affecting the binding of the second substrate (*10*, *11*). A critical step in the reaction mechanism seems to involve the distortion of the porphyrin macrocycle to a nonplanar conformation (*1*, *3*). Evidence for this distortion comes from resonance Raman spectroscopy of *Saccharomyces cerevisiae* (*12*) and murine (*13*) ferrochelatases. *S. cerevisiae* ferrochelatase, which lacks the [2Fe-2S] cluster, strained the porphyrin ring toward a domed conformation upon binding the potent inhibitor Hg^{2+} (*12*), whereas murine ferrochelatase, which contains the [2Fe-2S] cluster, distorted the porphyrin toward a ruffled conformation even in the absence of a metal substrate or inhibitor (*13*). Furthermore, the X-ray crystal structure of the *Bacillus subtilis* ferrochelatase with bound inhibitor *N*-methylmesoporphyrin indicated porphyrin distortion with a significant (36°) tilting of pyrrole ring A and fixing of the other three

† This work was supported by the American Cancer Society (Grant RPG-96-051-04-TBE) and American Heart Association, Florida Affiliate (Grant 0051240B), FLAD−Luso American Development Foundation (to G.C.F. and R.F.), and Fundação para a Ciência e Tecnologia (POCTI/34973/BME/2000) (to R.F.). The Stanford Synchrotron Radiation Laboratory is funded by the Department of Energy, Offices of Basic Energy Sciences and Biological and Environmental Research, the National Institutes of Health, National Center for Research Resources, Biomedical Technology Program, and the National Institute of General Medical Sciences.

* To whom correspondence should be addressed [G.C.F.: telephone, (813)-974-5797; fax, (813)-974-0504; e-mail, gferreir@hsc.usf.edu. G.N.G.: telephone, (650)-926-4604; fax, (650)-926-4100; e-mail, g.george@stanford.edu].

‡ University of South Florida.

§ Present address: Departamento de Química, Centro de Química Fina e Biotecnologia, Faculdade de Ciências e Tecnologia, Universidade Nova de Lisboa, 2825-114 Caparica, Portugal.

⊥ Stanford Synchrotron Radiation Laboratory.

10.1021/bi015814m CCC: $22.00
Published on Web 03/19/2002

pyrroles of the macrocycle, suggesting that the substrate metal ions access the porphyrin via the tilted pyrrole (*14*).

The nature of the binding of the substrate metal prior to insertion into the porphyrin is of key importance in understanding the catalytic mechanism of ferrochelatases, and it might be expected that the metal ion binding site would be adjacent to that of the porphyrin. Mössbauer spectroscopy of Fe^{2+} bound to the enzyme provides a direct probe of this and indicates a high-spin Fe^{2+} ion possessing nitrogen and/or oxygen ligands with no evidence of sulfur donors (*15*). The nature of the metal binding has also been investigated by the preparation of site-directed mutants. Histidine 207 (murine numbering) is conserved among all ferrochelatases and was the first residue suggested to be involved in iron binding (*16*). This was based on a decreased Fe^{2+} K_m in variants of the human enzyme in which this residue was mutated (*16*) and upon the almost undetectable activity of the corresponding *S. cerevisiae* H235 variants (*17*). Gora et al. also found evidence that in *S. cerevisiae* ferrochelatase D246 and Y248 (murine D218 and Y220) are involved in metal ion binding in a "synergistic manner" (*17*). Recently, the proposed role of H207 has been questioned and an alternate function for this residue suggested by Dailey and co-workers (*18*). These workers postulated that H207, which is positioned adjacent to the porphryin-binding cleft (*19*), functions as a proton acceptor for the porphyrin protons, which might then be shuttled to the surface of the protein via a series of negatively charged residues. The primary evidence for this new role is an X-ray crystallographic analysis in which Co^{2+} binding was observed at a site remote from both H207 and the porphyrin-binding cleft (*19*).

Here we present an X-ray absorption spectroscopic study of the substrate−metal binding site of ferrochelatase. We have studied both murine and *S. cerevisiae* (referred to hereafter as yeast) enzymes as examples of ferrochelatases containing and lacking the [2Fe-2S] cluster, respectively. The yeast ferrochelatase was reacted with Fe^{2+}, the enzyme's natural substrate, and also with Co^{2+} and Zn^{2+}, two of the divalent cations that have proven to be substrates in vitro. These metal ions were also used to probe the active site of murine ferrochelatase and of three of its variants: two variants of histidine 207 (H207N and H207A) and a variant in which tyrosine 220 was mutated to a phenylalanine (Y220F).

MATERIALS AND METHODS

Materials. Restriction enzymes and $Vent_R$ DNA polymerase were obtained from New England Biolabs and used according to the suppliers' instructions. Oligonucleotide primers were synthesized by Cybersyn, Inc., Lenni, PA, and Gibco BRL. Sequenase and the sequencing kit were from U.S. Biochemical Corp. [α-^{35}S]dATP was from Dupont/NEN Research Products. Acrylamide and gel reagents were purchased from Bio-Rad. The bicinchoninic acid protein assay reagents were obtained from Pierce Chemical Co. The QIAquick PCR purification kit was purchased from QIAGEN. Blue Sepharose and Superdex 200 resins were from Pharmacia. All other chemicals were of the highest purity available.

Construction of Variant Murine Ferrochelatase Plasmids. Plasmid pAP1, which contains the murine H207N ferrochelatase variant cDNA sequence under the control of the alkaline phosphatase promoter, was constructed as previously described for plasmid pAP4 encoding the E287Q variant (*20*). The construction of the H207A-encoding plasmid (pAM8) and Y220F-encoding plasmid (pAM9) was based on a PCR site-directed mutagenesis method, which involved three PCRs, as previously described for plasmid pAM6 encoding the E287A variant. (*20*).

Overproduction and Purification of Wild-Type and Variant Murine Ferrochelatase Forms. The wild-type and variant murine enzymes were overproduced in the *Escherichia coli* DH5α host strain harboring the different expression plasmids (i.e., pGF42, pAP1, pAM8, and pAM9) and purified to homogeneity according to the method previously described (*21*). The purified proteins were subsequently concentrated in a stirred cell with an YM 30 Diaflo ultrafiltration membrane (Amicon) and subjected to gel filtration chromatography by HPLC (Perkin-Elmer series 200) on a XK16 column (Pharmacia) packed with Superdex 200 (1.6 × 50 cm), to minimize the amount of cholate. The purified protein was eluted with buffer H (20 mM Tris-HCl, pH 8, 0.5 M NaCl, and 10% glycerol). The eluted protein fraction was then concentrated as described above and kept in liquid nitrogen until further use.

Overproduction and Purification of Wild-Type Yeast Ferrochelatase. The wild-type yeast enzyme was overproduced in *E. coli* DH5α cells harboring an yeast expression plasmid (*17*) and purified to homogeneity following the procedure developed by Camadro and Labbe (*22*). Briefly, the cells were grown and induced for the production of recombinant protein as previously described (*21*). The induced cells were then harvested by centrifugation. All purification procedures were carried out at 4 °C unless otherwise stated. The cells were resuspended in buffer F (20 mM Tris-HCl, pH 8, and 10% glycerol) containing 10 μg/mL PMSF, lysed in a French press cell (two passages at 12000 psi), and subjected to ultracentrifugation at 100000*g* for 45 min. The resulting supernatant was loaded onto a Blue Sepharose column (2.5 × 7 cm), previously equilibrated with equilibration buffer (1% Triton X-100 and 0.5 M NaCl in buffer F). The column was washed with equilibration buffer until the eluate had a value for A(280 nm) <0.1, followed by wash I buffer (1% Triton X-100 and 1 M NaCl in buffer F), buffer F, and wash II buffer (0.5% sodium cholate in buffer F). Elution of the yeast protein was accomplished with buffer F containing 1% sodium cholate and 1 M NaCl. The fractions containing yeast ferrochelatase were pooled and concentrated using a stirred cell with a YM30 Diaflo ultrafiltration membrane (Amicon) and subjected to gel filtration chromatography as described above for the recombinant murine enzymes.

SDS−PAGE, Protein Concentration Determination, and Enzyme Activity Assay. Protein purity was estimated by SDS−PAGE (*23*) and was never less than 95%, and protein concentration determination was performed as described previously (*21*). Briefly, 15% acrylamide and 1.5 mm thick gels were used in SDS−PAGE, and protein concentrations were determined by the bicinchoninic acid assay using BSA as standard. The enzymatic activity was determined using the pyridine hemochromogen as described by Falk (*24*). Briefly, ferrochelatase (2.0 μM, final concentration) was incubated with deuteroporphyrin (117.5 μM) and ferrous iron

citrate (235 μM) in 0.065 M Tris-HCl containing 50 mM mercaptoethanol for 20 min at 25 °C. The final volume of the reaction mixture was 0.85 mL, and the reaction was stopped by mixing in 0.5 mL of 1 M NaOH. Pyridine (0.5 mL) was then added, the sample was divided into two equal volumes, and excess solid sodium hydrosulfite was added to one. The difference absorption spectrum (560−500 nm) of the oxidized and reduced sample was run, and the iron deuteroporphyrin formed was quantitated using an extinction coefficient of 15.3 mM^{-1} cm^{-1} (*24*).

XAS Samples. XAS samples were prepared in a Lucite cuvette. An appropriate volume of the aqueous solution of the metal ion (i.e., $CoCl_2$, $ZnCl_2$, and ferrous ammonium sulfate) was added to the protein in buffer H. Glycerol was added to a final concentration of approximately 20% (v/v) to prevent artifacts due to ice diffraction. The Fe^{2+}-reacted samples were prepared anaerobically in order to avoid oxidation of the ferrous iron. The protein concentration in the XAS samples was close to 1 mM in all cases, and the protein:metal ion ratio was 1:1. Assuming that the metal K_m values for iron and zinc approximate the metal binding constants for Fe^{2+} (*19*) and Zn^{2+} (*25*), this metal concentration is expected to yield close to 100% bound form. No estimates of K_m or binding constant are available for Co^{2+}; however, this is expected to be similar to Fe^{2+} (*8*), and our results (see below) definitively indicate binding to histidine, which would only occur with close to 100% bound Co^{2+}.

X-ray Absorption Spectroscopy. Measurements were carried out at the Stanford Synchrotron Radiation Laboratory with the SPEAR storage ring containing 60−100 mA at 3.0 GeV, on beamlines 9-3 and 7-3 operating with a wiggler field of 2 and 1.8 T, respectively, and using a Si(220) double crystal monochromator. Beamline 9-3 is equipped with a Rh-coated collimating mirror upstream of the monochromator and a bent cylindrical Rh-coated focusing mirror downstream of the monochromator. Harmonic rejection was accomplished by setting the cutoff energy of the focusing mirror to 11 keV. The incident X-ray intensity was monitored using a nitrogen-filled ionization chamber, and X-ray absorption was measured as the X-ray Kα fluorescence excitation spectrum using an array of 30 germanium intrinsic detectors (*26*). During data collection, samples were maintained at a temperature of approximately 10 K using a liquid helium flow cryostat. For each sample between six and ten 35 min scans were accumulated, and the absorption of a standard metal foil was measured simultaneously by transmittance. The energy was calibrated with reference to the lowest energy inflection points of the metal foil standards, which were assumed to be 7111.3, 7709.5, and 9660.7 eV for Fe, Co, and Zn, respectively.

The extended X-ray absorption fine structure (EXAFS) oscillations $\chi(k)$ were quantitatively analyzed by curve fitting using the EXAFSPAK suite of computer programs (*27*) as described by George et al. (*28*), using ab initio theoretical phase and amplitude functions calculated using the program FEFF version 8.2 (*29*, *30*).

RESULTS AND DISCUSSION

Activity Measurements. All protein preparations were routinely verified for enzyme activity. Both the yeast and murine enzymes were fully active. The murine H207N and H207A variants exhibited undetectable enzymatic activity, whereas the Y220F variant was revealed to be as active as the wild-type murine ferrochelatase.

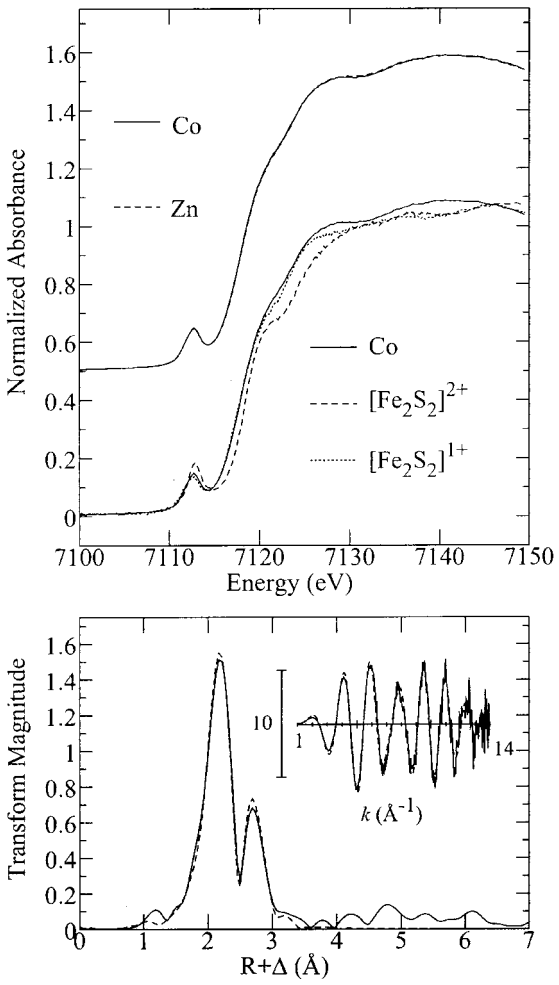

FIGURE 1: Upper panel: Iron K near-edge spectra of Co^{2+}- and Zn^{2+}-reacted wild-type murine ferrochelatase. The upper pair of near-edge spectra compares the spectra of Co^{2+} and Zn^{2+} murine ferrochelatase, and the lower set of spectra compares the Co^{2+} enzyme with the spectrum of *Anabaena* PCC719 ferredoxin in oxidized $[2Fe\text{-}2S]^{2+}$ and reduced $[2Fe\text{-}2S]^{1+}$ forms. Lower panel: Iron K-edge EXAFS Fourier transform and k^3-weighted EXAFS spectra (inset) of Zn^{2+}-reacted wild-type murine ferrochelatase. The solid lines show experimental data, and the broken lines show best fits. Parameters obtained were four Fe−S at 2.267(2) Å with mean-square deviation in distance (σ^2) of 0.0051(3) Å^2, one Fe−Fe at 2.740(3) Å with a σ^2 of 0.0023(3) Å^2, and a threshold shift ΔE_0 of −7.8(5) eV, where the values in parentheses are the estimated standard deviations obtained from the diagonal elements of the covariance matrix. The Fe K-edge EXAFS spectrum of Co^{2+}-reacted murine ferrochelatase (not illustrated) was identical within the noise of the data. The Fourier transforms have been phase-corrected for Fe−S backscattering.

The Iron−Sulfur Center of Murine Ferrochelatase. The iron−sulfur cluster of animal ferrochelatases has been the focus of several previous studies. The crystal structure of the human enzyme (*19*) shows a conventional [2Fe-2S] cluster core, although it is bound solely by the four cysteine thiolate ligands to iron and lacking the usual hydrogen bonding from amino acid residues to iron and sulfur atoms. Figure 1 shows the iron K near-edge of the Co^{2+}- and Zn^{2+}-reacted wild-type murine ferrochelatase (upper panel). The upper pair of traces compare the spectra of the [2Fe-2S]

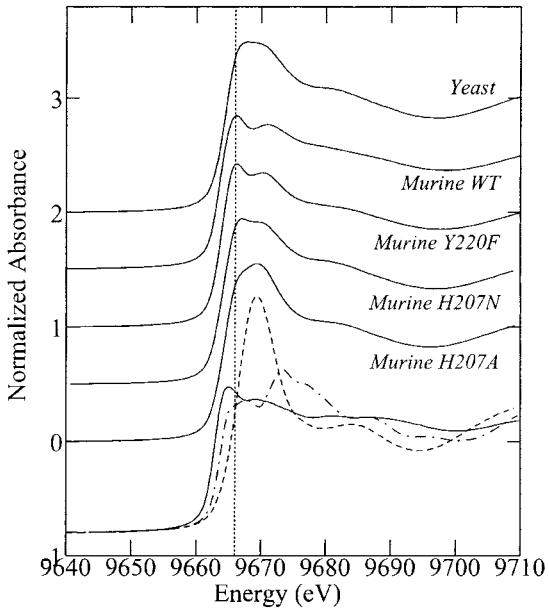

FIGURE 2: Zinc K near-edge spectra for Zn^{2+}-reacted ferrochelatases. The lowest three plots compare model spectra for zinc-substituted *Pyrococcus furiousus* rubredoxin (solid line), tetraimidazole Zn^{2+} bisnitrate (dot−dashed line), and hexaquo Zn^{2+} bisnitrate (dashed line). The vertical dotted line at 9666.0 eV is shown to guide the eye to relative changes in the edge spectra.

cluster from the Co^{2+}- and Zn^{2+}-reacted enzyme. The spectra are identical, indicating that either the reaction with Co^{2+} and Zn^{2+} induces no changes in the structure of the iron−sulfur cluster or that the metals induce the same change. The bottom three traces compare the Fe K near-edge spectrum of the [2Fe-2S] cluster in the Co^{2+}-reacted enzyme, with the spectrum of *Anabaena* PCC719 ferredoxin in oxidized $[2Fe\text{-}2S]^{2+}$ and reduced $[2Fe\text{-}2S]^{+}$ forms. It is clear that the ferrochelatase iron−sulfur near-edge spectrum most closely resembles that of the reduced $[2Fe\text{-}2S]^{+}$ cluster. Although the sample was initially oxidized, significant presence of the reduced species is expected from photoreduction by the high-intensity X-ray beams available on beamline 9-3. For both Co^{2+} and Zn^{2+} ferrochelatases, the Co and Zn XAS data (see below) were collected prior to collection of the Fe XAS data, so that the sample had been exposed to the X-ray beam for approximately 4 h before the first Fe data set was collected. Since approximately 1 h of exposure to the 9-3 X-ray beam is sufficient to significantly photoreduce many metalloproteins, the presence of a photoreduced $[2Fe\text{-}2S]^{+}$ in ferrochelatase is not unexpected. The lower panel in Figure 1 shows the Fe K-edge EXAFS curve fitting of Zn^{2+}-reacted wild-type murine ferrochelatase. The analogous data from the Co^{2+}-reacted protein are quantitatively identical. Curve-fitting parameters were four Fe−S at 2.27 Å and one Fe−Fe at 2.74 Å, which are typical of a [2Fe-2S] cluster (*31*).

Zn^{2+}-Reacted Ferrochelatases. Figure 2 shows the Zn K near-edge spectra of yeast, murine wild type, and three different murine site-directed mutants, compared with spectra from tetrahedral Zn−S and Zn−N species, and an octahedral Zn−O complex. Although the enzyme spectra are all different from each other, they are broadly similar, quite distinct from the octahedral model, and appear to be intermediate between the tetrahedral Zn−S and Zn−N models. For the murine enzyme, mutation of Y220 and H207

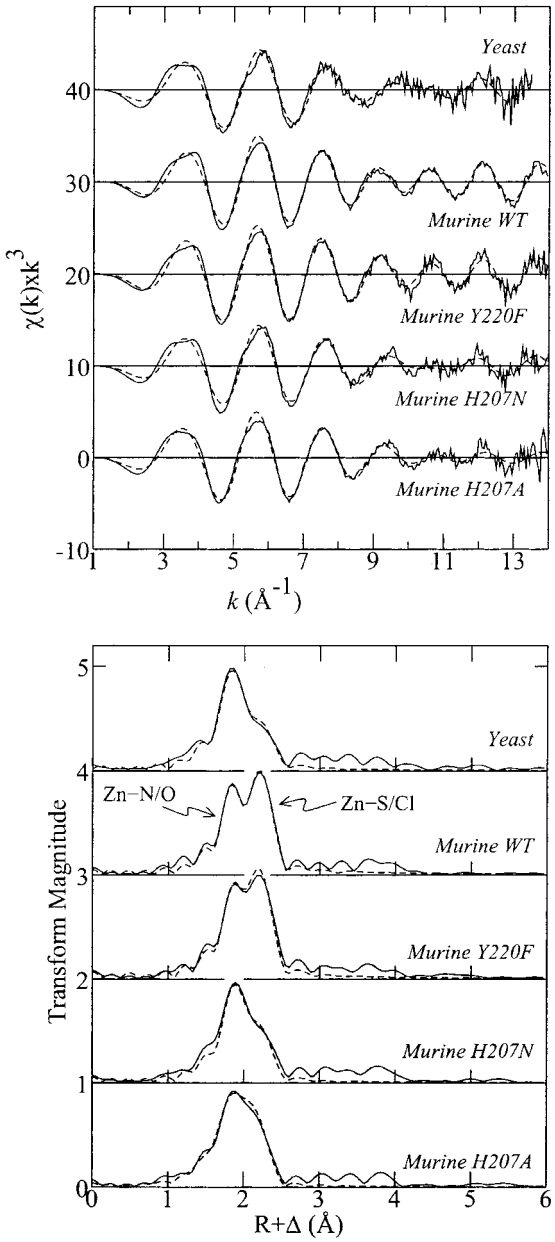

FIGURE 3: Zinc K-edge EXAFS (upper panel) and EXAFS Fourier transforms (lower panel) of Zn^{2+}-reacted yeast and murine ferrochelatases. The solid lines show experimental data and the broken lines the best fits. The Fourier transforms have been phase-corrected for Zn−O backscattering.

to residues which are (potentially) noncoordinating changes the spectra, although with Y220F this change is quite subtle. Interestingly, the spectrum of the murine H207N site-directed mutant is more similar to that of the yeast enzyme than is the murine wild type. These data indicate that the Zn site is not six coordinate and suggest that it may be four coordinate (tetrahedral) with mixed Zn−S/Cl and Zn−N/O ligation.

Figure 3 shows the Zn K-edge EXAFS oscillations, EXAFS Fourier transforms, and best fits for the Zn^{2+}-reacted ferrochelatase samples. EXAFS cannot readily distinguish between scatterers of similar atomic number, such as oxygen and nitrogen, or sulfur and chlorine, although oxygen and sulfur (for example) are usually easy to tell apart. The curve-fitting analysis is summarized in Table 1 and indicates mixed Zn−N/O and Zn−S/Cl coordination giving rise to the two major Fourier transform peaks (Figure 3). The small trans-

Table 1: EXAFS Curve-Fitting Results for Zn^{2+}-Reacted Ferrochelatases[a]

	Zn−N/O			Zn−S/Cl				
sample	*N*	*R*	σ^2	*N*	*R*	σ^2	ΔE_0	*F*
yeast	3	1.972(4)	0.0048(3)	1	2.275(5)	0.0039(3)	−17.8(8)	0.378
murine WT	2	1.973(2)	0.0037(2)	2	2.282(2)	0.0040(1)	−16.7(3)	0.206
murine Y220F	2	2.002(3)	0.0026(2)	2	2.286(3)	0.0031(1)	−12.1(6)	0.269
murine H207N	3	1.995(4)	0.0050(2)	1	2.286(4)	0.0037(3)	−15.6(7)	0.314
murine H207A	3	1.997(4)	0.0053(2)	1	2.273(4)	0.0026(2)	−18.1(7)	0.302

[a] Coordination numbers (*N*); interatomic distances (*R*) are given in Å, Debye−Waller factors (σ^2) (the mean-square deviations in interatomic distance) are in Å^2, and the threshold energy shifts (ΔE_0) are given in eV. The values in parentheses are the estimated standard deviations obtained from the diagonal elements of the covariance matrix. The fit error function *F* is defined as $\{\sum k^6(\chi_{calc} - \chi_{expt})^2/\sum \chi_{expt}^2\}^{1/2}$. The best fits are presented; alternatives involving different total coordination numbers were tested for all samples and gave substantially worse fits and in some cases physically unreasonable Debye−Waller factors.

form peaks between 2.8 and 4.0 Å are due to outer shell carbons and/or nitrogens, possibly due to histidine coordination. These outer shell EXAFS are complex, giving rise to at least four small transform peaks (Figure 3), and lack the distinctive two-peak pattern normally observed with histidine ligands, although we note that this could be due to geometrical irregularities (see below). No attempt was made to fit these low-intensity outer shell features. EXAFS curve-fitting analysis gives very accurate bond lengths *R* for directly coordinated atoms (typically better than ±0.02 Å) and much less accurate coordination numbers, *N*, and Debye−Waller factors, σ^2 (typically around ±25%). The reason for this is a high mutual correlation of *N* and σ^2 in the refinement, and it is thus unwise to simultaneously refine these parameters; we adopt the more acceptable practice of restricting *N* to integer values, refining σ^2, and comparing the best fits. Curve fitting of the first shell EXAFS indicates four-coordinate sites, with either one or two Zn−S/Cl ligands and three or two Zn−N/O ligands, depending upon the sample.

The zinc coordination of the yeast and the wild-type murine enzyme is different, with $Zn(N/O)_3(S/Cl)_1$ coordination for the yeast and $Zn(N/O)_2(S/Cl)_2$ coordination for the murine enzyme. Furthermore, the Y220 and H207 murine site-directed mutants change both the EXAFS and the near-edge spectra. For the Y220F variant the coordination remains the same, with subtle changes in the near-edge spectrum (Figure 2) and in the bond lengths (Figure 3, Table 1). In the case of H207 variants the coordination is changed from a $Zn(N/O)_2(S/Cl)_2$ to a $Zn(N/O)_3(S/Cl)_1$; i.e., the site has lost a S or Cl ligand and now resembles the yeast enzyme. This is best defined in the data for H207N, which show strong similarities of both near-edge and EXAFS spectra to the yeast enzyme (Figures 2 and 3).

We now address the possible identity of the ligands. It is possible that the Zn−S/Cl ligands are in fact Zn−Cl derived from chloride in the buffer and the Zn−N/O ligands may be either nitrogen or oxygen from amino acid side chains or possibly a water oxygen. A search of the Cambridge structural database (*32*) indicated that the EXAFS-derived bond lengths are more typical of Zn−O and Zn−S coordination than of Zn−Cl and Zn−N coordination. Thus, $ZnCl_2N_2$ coordination gave average Zn−Cl and Zn−N bond lengths of 2.23 and 2.05 Å, respectively, and ZnS_2O_2 coordination gave average Zn−S and Zn−O bond lengths of 2.30 and 1.99 Å, respectively. The latter values compare well with the values derived from EXAFS of the wild-type murine enzyme of Zn−S at 2.28 Å nd Zn−O at 1.97 Å. For all permutations of Cl, S, N, and O coordination, the bond lengths of the enzyme-bound zinc were more similar to the averages of the database values for S and O than for Cl and N. Water ligands exhibited longer than average Zn−O bond lengths (2.08 Å) and were therefore more similar to Zn−N. We note that these trends cannot definitively identify the ligands, as the ranges of Zn−S versus Zn−Cl and Zn−O verses Zn−N bond lengths overlap somewhat.

Examination of the crystal structure of the human enzyme indicates that there is one cysteine residue in the vicinity of the proposed site for Co^{2+} binding (*19*), but there are no candidates for biscysteine coordination anywhere in the structure. On the basis of this fact, a bischloride coordination seems most probable. The fact that mutation of the conserved residues Y220 and H207 causes changes in the coordination of the metal suggests that the metal is bound in proximity to these residues, rather than at the proposed cobalt binding site (*19*), which is some 20 Å from H207 and Y220. Our data suggest that Y220 is unlikely to be directly coordinated to the metal as the changes in spectra in the Y220F variant are quite subtle. The finding of probable chloride ligands to zinc was an unexpected aspect of our results, and the decrease in S/Cl coordination caused by mutation of H207 is difficult to rationalize. The possibility that Zn^{2+} might not be bound to the active site in the H207 murine variants must be considered. Setting details aside, one important finding of our studies is that the coordination environment of Zn^{2+} in both murine and yeast ferrochelatases is quite different to that of Fe^{2+} in yeast ferrochelatase (see below). This and the other differences in coordination suggest that Zn^{2+} is not a good model of the binding of the native substrate, Fe^{2+}, and we will not consider it further.

Co^{2+}-Reacted Ferrochelatases. Figure 4 shows the Co K near-edge spectra of yeast, murine wild type, and two murine site-directed mutants (Y220F and H207N), together with the spectra of two different Co^{2+} model compounds. The models are the octahedral $Co(H_2O)_6(NO_3)_2$ and the (approximately) square-planar four-coordinate (*meso*-tetraphenylporphinato)-cobalt(II) (*33*). All of the enzyme spectra are quite similar to each other and clearly resemble the octahedral model compound spectrum. Thus, in marked contrast to the zinc data, the near-edge data indicate a six-coordinate binding site for Co^{2+}. The EXAFS spectra plus corresponding Fourier transforms together with best fits from curve-fitting analysis are shown in Figure 5, and Table 2 gives details of the analysis. In all of these cases the EXAFS are dominated by a first-shell interaction that gives rise to the intense Fourier transform peak at 2.1 Å, and EXAFS curve-fitting analysis indicates six oxygen or nitrogen ligands at about this distance.

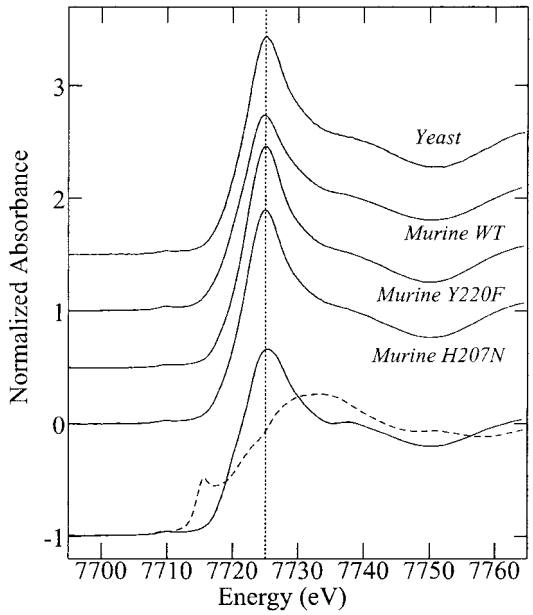

FIGURE 4: Cobalt K near-edge spectra for the Co^{2+}-reacted ferrochelatases. Top to bottom: yeast, wild-type murine, murine Y220F, and murine H207N. The bottom two traces compare the near-edge spectra of two models, the approximately octahedral $Co(H_2O)_6(NO_3)_2$ (solid line) and the approximately square planar four-coordinate species (*meso*-tetraphenylporphinato)cobalt(II) (broken line). The vertical dotted line at 7725.04 eV is shown to guide the eye to relative changes in the spectra.

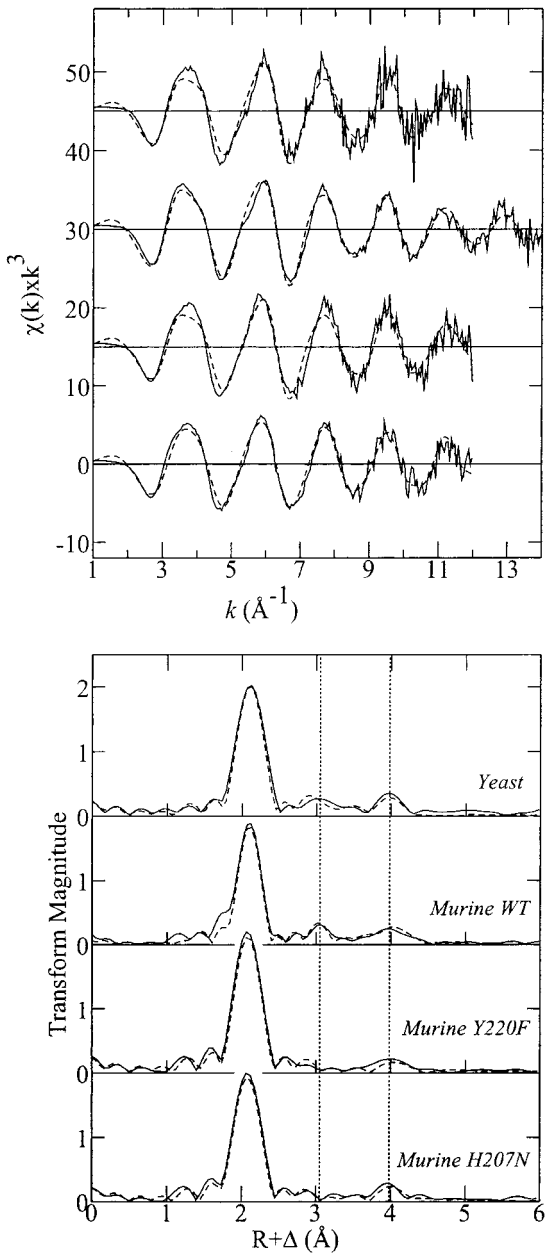

FIGURE 5: Cobalt K-edge EXAFS (upper panel) and EXAFS Fourier transforms (lower panel) of Co^{2+}-reacted ferrochelatases. From top to bottom: yeast, murine wild type, murine Y220F, and murine H207N. The solid lines show experimental data and the broken lines the best fits. The Fourier transforms have been phase-corrected for Co−O backscattering, and the parameters obtained in the curve-fitting are given in Table 2. The vertical dotted lines at $R + \Delta = 3.05$ and 3.98 Å are shown in the Fourier transform figure to guide the eye with respect to the long-distance imidazole peak positions.

The small Fourier transform peaks at about 3 and 4 Å are typical of histidine coordination, arising from backscattering of the outer shell carbons and nitrogens of the histidine imidazole ring. The yeast and murine wild type are very similar, with well-defined transform peaks at 3 and 4 Å, but the Y220F and H207N murine variants show differences, with a diminised 3 Å peak intensity. Outer shell EXAFS with contributions from multiple scattering from imidazole coordination have been well studied for copper proteins (*34*, *35*) and are very sensitive to the ring orientation with respect to the metal (*34*). Figure 6 shows this sensitivity for an idealized Co−imidazole complex. The model was generated using the average ring dimensions of all cobalt−imidazole entries in the Cambridge structural database (*32*), and two different angles (α and β in Figure 6) were systematically varied. Quite small values of α (e.g., 5°) can effectively eliminate the 3 Å tranform peak, while the 4 Å peak remains. A larger (25°) variation in β has the opposite effect of eliminating the 4 Å peak, leaving the 3 Å peak. The full multiple scattering treatment of the histidine (*36*) outer shell fits well to the Co^{2+} enzyme EXAFS data, and in all cases two histidines are needed to satisfy the outer shell intensity, although a rotated ($\alpha = 5°$) imidazole ring was required for the murine Y220F and H207N variants. Although the imidazole ring is not symmetric, the sign of the rotation made very little difference to the fits (i.e., $\alpha = +5°$ and $\alpha = -5°$ were essentially equivalent). We note in passing that this result indicates that the presence of significant levels of unbound Co^{2+} cannot be present.

Uncertainty in the Debye−Waller factors (σ^2 values) can add a large number of variables in an EXAFS multiple scattering analysis, as each scattering path has an associated σ^2. Recent developments in theory (*36*) have allowed us to minimize the number of variables by calculating the vibrational contributions to the Debye−Waller factor. The Debye−Waller factor typically has both vibrational and static contributions ($\sigma^2 = \sigma^2_{vib} + \sigma^2_{stat}$), and the latter arise from differences in interatomic distances that are less than the EXAFS resolution (of about 0.1 Å). We calculated the σ^2_{vib} values for the imidazole ligand using the method of Poiarkova and Rehr (*36*) and held these values fixed during the refinements. The relative interatomic distances for the imidazole ring were also held fixed during the refinements, and σ^2_{stat} together with the Co−N bond length were the only

Table 2: EXAFS Curve-Fitting Results for Co^{2+}- and Fe^{2+}-Reacted Ferrochelatases[a]

	Co−O/N			Co−imidazole						
sample	*N*	*R*	σ^2	*N*	*R*	σ^2_{stat}	α	*k* range	ΔE_0	*F*
yeast Co	4	2.129(4)	0.0020(3)	2	2.049(8)	0.0010(1)	0	1−12	−1.9(8)	
murine WT Co	4	2.127(2)	0.0029(2)	2	2.047(6)	0.0041(8)	0	1−14	−2.0(5)	0.213
murine H207N Co	4	2.095(4)	0.0032(5)	2	2.085(9)	0.0020(5)	5	1−12	−2.0(4)	0.270
murine Y220F Co	4	2.077(3)	0.0024(2)	2	2.137(9)	0.0010(5)	5	1−12	−2.1(4)	0.268

	Fe−O/N			Fe−imidazole						
sample	*N*	*R*	σ^2	*N*	*R*	σ^2_{stat}	β	k_{max}	ΔE_0	*F*
yeast Fe	4	2.002(2)	0.0043(3)	2	2.117(5)	0.0010(5)	20	1−12	−1.1(3)	0.231

[a] Coordination numbers (*N*); interatomic distances (*R*) are given in Å, Debye−Waller factors (σ^2) (the mean-square deviations in interatomic distance) are in $Å^2$, the angles α and *β* are in degrees, the *k* -range is in $Å^{-1}$, and the threshold energy shifts (ΔE_0) are given in eV. The values in parentheses are the estimated standard deviations obtained from the diagonal elements of the covariance matrix. The fit error function *F* is defined as $\{\sum k^6(\chi_{calc} - \chi_{expt})^2/\sum \chi_{expt}^2\}^{1/2}$. Coordination numbers *N* and the angles α and *β* were held fixed in the refinements, and individual refinements with different integer values of *N* (and selected values of α and *β*) were compared. In all cases the best fit obtained is given in the table.

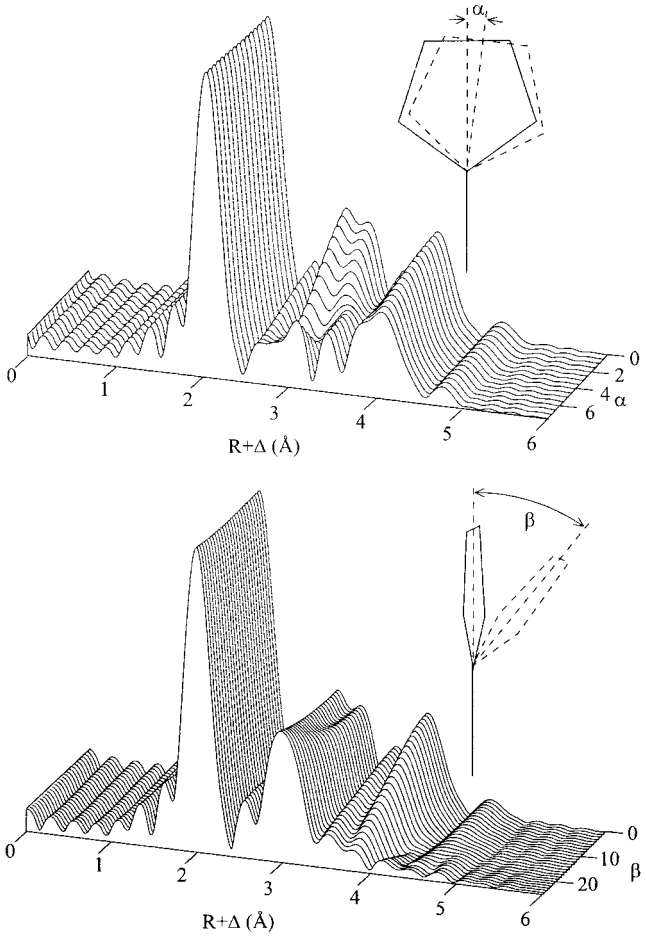

FIGURE 6: Calculated Co K-edge EXAFS Fourier transforms (Co−N phase-corrected, *k* range = 1−14 $Å^{-1}$) for different imidazole coordination geometries. The upper panel shows the effects of rotating the imidazole ring through the angle α, about a vector normal to the plane of the imidazole ring. The lower panel shows the effects of rotating the imidazole ring through the angle *β*, about a vector normal to both the Co−N bond and the normal to the ring plane. All scattering paths were included, and the Debye−Waller factors were calculated as described in the text.

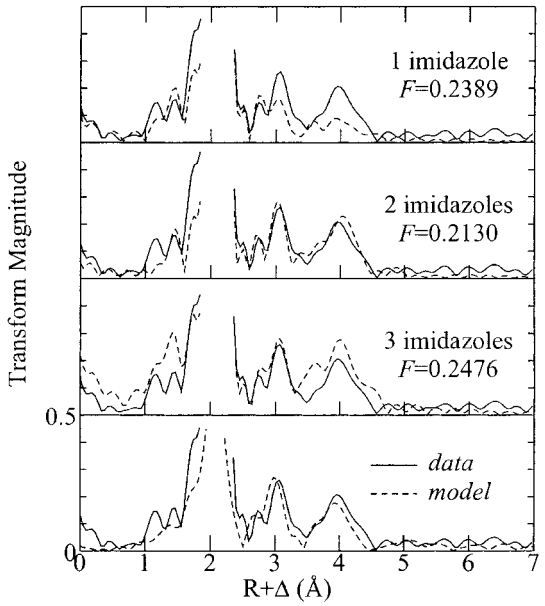

FIGURE 7: Optimization of the number of coordinated histidines for wild-type murine ferrochelatase. The outer shell contributions to the Fourier transforms (Co−N phase-corrected) are shown with fits to one, two, and three imidazole ligands to cobalt. In all cases the solid line shows experimental data and the broken line the best fit. The first shell coordination was not changed between fits, and the σ^2_{stat} values were restrained within chemically reasonable bounds (i.e., between 0 and 0.01 $Å^2$). The fit errors (*F* values) for each fit are given in the figure. The bottom pair of Fourier transforms compares murine ferrochelatase (solid line) with a model compound with four imidazole ligands (broken line). The amplitude of the model spectrum has been reduced by a factor of 2 to show the Fourier transform peak intensity expected for two coordinated imidazole ligands and can be seen to be very similar to the peak intensity observed for ferrochelatase.

variables needed for fitting the whole group. In our calculations we used the force constants for the imidazole ring employed by Poiarkova and Rehr (*36*) and assumed a force constant for the Co−N bond of 130 N/m (estimated from DGauss density functional theory). Thus, for fitting histidine ligands, the best fits for different fixed values of coordination number, α, and *β* were compared, refining the Co−N bond length and σ^2_{stat} value for each, along with the bond length and σ^2 value of the other ligands (Table 2). The optimization of the number of imidazole outer shell contributions is shown in Figure 7 for the murine wild-type enzyme, together with a comparison of the Fourier transform of a model with coordinated imidazole rings (*37*). A search of the Cambridge Crystal Structure Database (*32*) for six-coordinate CoN_2O_4 species gave an average Co−O/N bond length of 2.04 Å, whereas five-coordinate CoN_2O_3 and four-coordinate CoN_2O_2

species gave average bond lengths of 1.97 and 1.90 Å, respectively. The Co−O/N distance (Table 2) is therefore reasonable for a six-coordinate cobalt species with nitrogen and oxygen ligands, and the near-edge spectra (Figure 4) are typical of octahedral coordination.

The Co^{2+}-reacted form of the human enzyme has been studied by X-ray crystallography (*19*). In this study, a cobalt binding site was identified approximately 20 Å from the proposed heme binding site, with one (*18*) or possibly two (*19*) histidine ligands (H230 and H231, human numbering) and an aspartate (D383, human), with the remainder of the coordination presumably made up by water ligands. While the aspartate residue is conserved between human, murine, and yeast ferrochelatases, this is not true of the two histidine ligands. Only one of the two potential histidine ligands is conserved in the mouse protein (H193), the other being replaced by a proline residue (P194). In the yeast protein, the two histidines are replaced by asparagine and glutamate. Thus, the cobalt binding site in the yeast and murine enzymes is unlikely to be the same site observed crystallographically for human ferrochelatase. Other candidate sites with potential bishistidine coordination must therefore be considered. Assuming that the murine protein has a structure similar to that determined crystallographically for the human enzyme (*19*), the only conserved pairs of histidine residues that are located close enough to both bind to a metal are H110 and H332 (H157 and H388, human) and H207 and H285 (H263 and H341, human). The H110/H332 site is remote from the proposed porphyrin-binding site, while the H207/H285 site is very close. It is possible that the latter site binds cobalt in wild-type murine enzyme, while the former binds the metal in the murine H207N variant and perhaps the Y220F variant as well. H207 has previously been suggested to bind metal prior to insertion into the porphyrin ring, but an alternative role in proton abstraction has also been proposed (*3*, *18*). In any case, it is clear from our data that both H207 and Y220 do influence the nature of cobalt binding in murine ferrochelatase, and both are thus candidate ligands. On the basis of the crystal structure of human ferrochelatase, H207 and Y220 are expected to be some 30 Å from the H110/H332 site, and any measurable effects at this distance seem unlikely.

Ferrous Iron-Reacted Yeast Ferrochelatase. Figure 8 shows the X-ray absorption spectroscopy of ferrous iron-reacted yeast ferrochelatase. The iron K near-edge spectrum, shown in Figure 8 (upper panel), resembles previously reported six-coordinate high-spin ferrous spectra (*38*), suggesting the presence of a six-coordinate site. The small feature near 7113 eV is the quadrupole-allowed 1s → 3d transition, which gains dipole-allowed intensity in noncentrosymmetric environments by admixture of 4p levels. The weak presence of this feature here argues for centrosymmetric (e.g., approximately octahedral) coordination of the metal.

The iron EXAFS spectrum is shown in Figure 7 and is dominated by Fe−N/O backscattering from approximately six ligands with an average bond length of 2.04 Å (Table 2). Five-coordinate Fe^{2+} is also possible, but four ligands give an unacceptable fit. The Fourier transform peaks at approximately 3 and 3.8 Å are from outer shells. As discussed above, outer shell features at about 3 and 4 Å are commonly seen with histidine ligands due to backscattering of the outer carbons and nitrogen of the imidazole ring, and

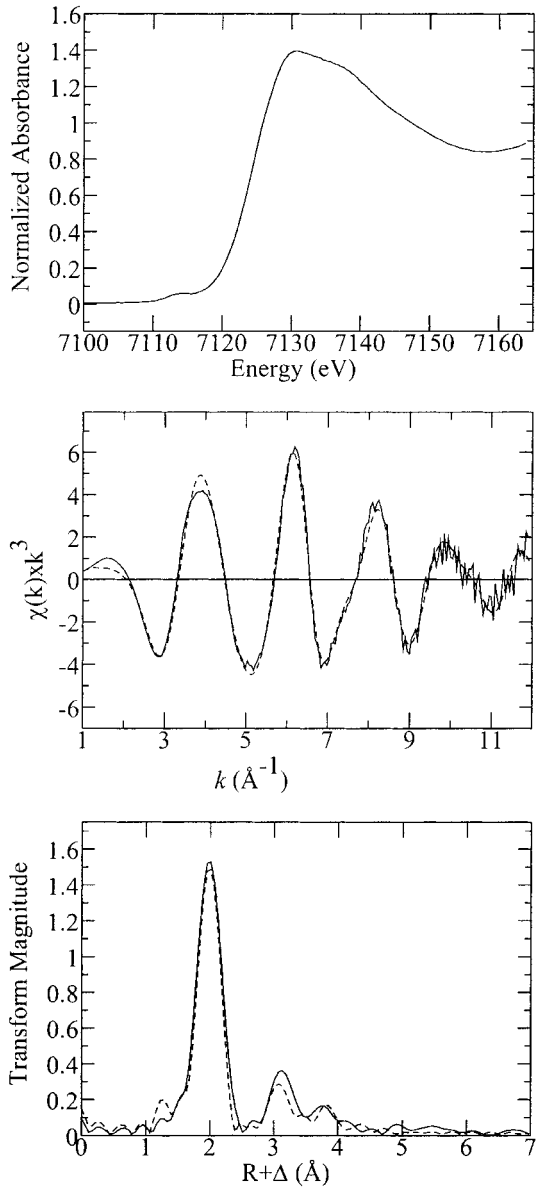

FIGURE 8: Iron K-edge X-ray absorption spectra of Fe^{2+}-reacted yeast ferrochelatase. The upper panel shows the iron K near-edge spectrum, the middle panel shows the EXAFS oscillations (solid line) and best fit (broken line),and the lower panel shows the corresponding EXAFS Fourier transforms (Fe−O phase-corrected). The parameters obtained in curve fitting are given in Table 2.

a model in which two histidines are bound with a tilted imidazole ring ($\beta = 20°$, Figure 6) fits the data well (Figure 8). This interpretation is in agreement with the results from Co^{2+}-bound enzyme, which indicate a bishistidine coordination, but a single sulfur or phosphorus at 3.22 Å fits almost as well (not illustrated), and although we consider this coordination unlikely, it cannot be unequivocally excluded on the basis of the EXAFS data alone.

Bond lengths typically change systematically with coordination number and can thus be used to provide additional information. A search of the Cambridge Crystal Structure Database (*32*) for six-, five-, and four-coordinate Fe−N/O species gave average bond lengths of 2.05, 2.00, and 1.97 Å, respectively. Thus, the bond length supports a six-coordinate site, in excellent agreement with the best fit obtained from the curve-fitting analysis (Table 2).

The coordination of the three different metal ions investigated in the present work is similar to that observed in other metalloproteins. Several mononuclear non-heme iron proteins possess five- or six-coordinate sites with no sulfur ligands, and only oxygen or nitrogen coordinated to the metal. Most often three histidine ligands are present, for example, in lipoxygenase (*39*, *40*) and in iron superoxide dismutates (*41*, *42*), but bishistidine coordination also occurs, for example, in isopenicillin *N*-synthase (*43*). Co^{2+}-substituted Fur (a regulatory protein that binds Fe^{2+} under physiological conditions) presents an axially distorted hexacoordinated geometry with two or three histidines and one or two oxygen-containing ligands (*44*). For Zn^{2+}, especially in the case of structural zinc sites, a tetrahedral coordination containing thiolate ligands (two to four) is by far the most common coordination environment (*45*).

Our data indicate that Co^{2+} and Fe^{2+} are bound to ferrochelatase in six or possibly five (in the case of Fe^{2+}) oxygen or nitrogen ligands, two of which are histidines, possibly one tyrosine (Y220), and probably two or three H_2O ligands. Such an extensive coordination with water is not common in other metalloproteins but is in accord with the role of the functional role of the ferrochelatase metal binding site. This site must give up the metal ion for insertion into the porphyrin, and very strong binding to the site, such as might be expected if more ligands were provided by amino acid side chains, is thus not desirable. Similarly, Zn^{2+} might not be expected to be a substrate if thiolate donors were present, as these might bind the metal too tightly, and this supports our conclusion of Cl^- coordination with this metal.

CONCLUSION

The evidence presented in this paper suggests that the metal binding site of murine and yeast ferrochelatase is different from that observed crystallographically for the human enzyme. Our results indicate a bishistidine coordination for iron in yeast ferrochelatase and cobalt in wild-type murine ferrochelatase, which is modified upon mutation of H207 and Y220. Setting aside any quantitative analysis, the simple observation of different spectra for H207 and Y220 variants strongly suggests a role of these residues in binding metal−substrate ions. This casts doubt upon the conclusions about metal binding derived from the crystal structure (*19*). Figure 9 shows a schematic rendition of the crystal structure of human ferrochelatase (*19*) indicating the three possible metal binding sites considered in the discussion above. The crystal structure showed cobalt bound to the enzyme at a site some 20 Å from H207 (human H263, site a in Figure 9) on the opposite side of the molecule from the porphyrin cleft, and it has been suggested that the metal is translocated from this site via a series of negatively charged residues (*18*, *19*). The crystal structure also showed the presence of three detergent (cholate) molecules in the proposed porphyrin-binding cleft. A calculation of the molecular surfaces (0.002 $Å^2$ electron density isosurfaces calculated using SPARTAN employing an AM1 Hamiltonian) indicates dimensions for the rigid parts of protoporphyrin IX and of cholate of 13.9 × 13.2 × 4.0 Å and 15.5 × 8.1 × 7.3 Å, respectively. Thus, the three bulky cholate molecules are together considerably larger than the protoporphyrin IX substrate, and it seems likely that their presence in the porphyrin cleft might have disrupted the native mode of metal binding in the crystallographic experiments.

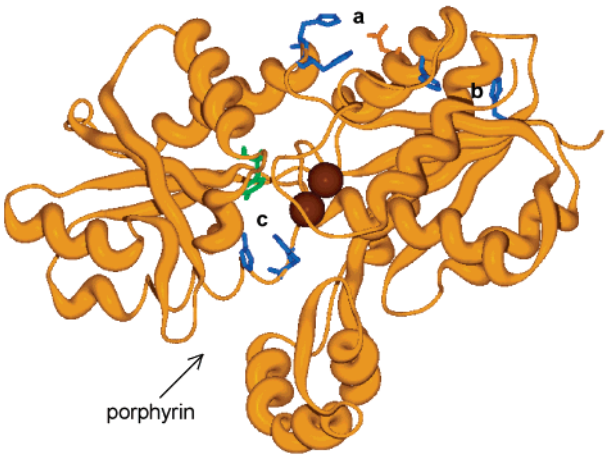

FIGURE 9: Schematic rendition of the crystal structure of human ferrochelatase. The figure was prepared using the protein data bank atomic coordinates with accession code 1HRK. The proposed porphyrin-binding cleft is indicated at the bottom left of the molecule. Three possible metal binding sites discussed in the text are indicated. Site a is the crystallographically observed site involving H230, H231, and D383 (human numbering), site b involving H157 and H388, and site c involving H263, H341, and Y276, human numbering). The colors used in the figure are blue for histidine, green for tryrosine, red for aspartate, orange for the polypeptide backbone, and brown for the iron atoms of the [2Fe-2S] cluster (shown in space-filling mode). The three cholate molecules contained in the porphyrin cleft have been omitted for clarity.

ACKNOWLEDGMENT

We thank Dr. Ingrid J. Pickering and Dr. Roger C. Prince for assistance with data acquisition.

REFERENCES

1. Franco, R., Lloyd, S. G., Moura, J. J. G., Moura, I., Huynh, B. H., and Ferreira, G. C. (1999) in *Inorganic Biochemistry and Regulatory Mechanisms of Iron Metabolism* (Ferreira, G. C., Franco, R., and Moura, J. J. G., Eds.) pp 35−50, Wiley-VCH, Weinheim.
2. Dailey, H. A. (1990) in *Biosynthesis of Heme and Chlorophylls* (Dailey, H. A., Ed.) pp 123−161, McGraw-Hill, New York.
3. Dailey, H. A., Dailey, T. A., Wu, C.-K., Medlock, A. E., Wang, K.-F., Rose, J. P., and Wang, B.-C. (2000) *Cell. Mol. Sci. Life 57*, 1909−1926.
4. Porra, R., and Jones, O. T. G. (1963) *Biochem. J. 87*, 181−185.
5. Ferreira, G. C., Franco, R., Lloyd, S. G., Pereira, A. S., Moura, I., Moura, J. J. G., and Huynh, B. H. (1994) *J. Biol. Chem. 269*, 7062−7065.
6. Dailey, H. A., Finnegan, M. G., and Johnson, M. K. (1994) *Biochemistry 33*, 403−407.
7. Day, A. L., Parsons, B. M., and Dailey, H. A. (1998) *Arch. Biochem. Biophys. 359*, 160−169.
8. Dailey, H. A., Jones, C. S., and Karr, S. W. (1989) *Biochim. Biophys. Acta 999*, 7−11.
9. Dailey, H. A., and Fleming, J. E. (1983) *J. Biol. Chem. 258*, 11453−11459.
10. Labbe-Bois, R., and Camadro, J.-M. (1994) in *Metal Ions in Fungi* (Winkelmann, G., and Winge, D., Eds.) pp 413−453, Marcel Dekker, New York.
11. Rossi, E., Attwood, P. V., Garcia-Webb, P., and Costin, K. A. (1990) *Biochim. Biophys. Acta 1038*, 375−381.

12. Blackwood, M. E., Jr., Rush, T. S., III, Romesberg, F., Schultz, P. G., and Spiro, T. G. (1998) *Biochemistry 37*, 779−782.
13. Franco, R., Ma, J. G., Lu, Y., Ferreira, G. C., and Shelnutt, J. A. (2000) *Biochemistry 39*, 2517−2529.
14. Lecerof, D., Fodje, M., Hansson, A., Hansson, M., and Al-Karadaghi S. (2000) *J. Mol. Biol. 297*, 221−232.
15. Franco, R., Moura, J. J. G., Moura, I., Lloyd, S. G., Huynh, B. H., Forbes, W. S., and Ferreira, G. C. (1995) *J. Biol. Chem. 270*, 26352−26357.
16. Kohno, H., Okuda, M., Furukawa, T., Tokunaga, R., and Taketani, S. (1994) *Biochim. Biophys. Acta 1209*, 95−100.
17. Gora, M., Grzybowska, E., Rytka, J., and Labbe-Bois, R. (1996) *J. Biol. Chem. 271*, 11810−11816.
18. Sellers, V. M., Wu, C.-K., Dailey, T. A., and Dailey, H. A. (2001) *Biochemistry 40*, 9831−9827.
19. Wu, C.-K., Dailey, H. A., Rose, J. P., Burden, A. M., Sellers, V. M., and Wang, B.-C. (2001) *Nat. Struct. Biol. 8*, 156−160.
20. Franco, R., Pereira, A. S., Tavares, P., Mangravita, A., Barber, M. J., Moura, I., and Ferrier, G. C. (2001) *Biochem. J. 356*, 217−222.
21. Ferreira, G. C. (1994) *J. Biol. Chem. 269*, 4396−4400.
22. Camadro, J.-M., and Labbe, P. (1988) *J. Biol. Chem. 263*, 11675−11682.
23. Laemmli, U. K. (1970) *Nature 227*, 680−685.
24. Falk, J. E. (1964) *Porphyrins and Metallporphyrins*, Elsevier, New York.
25. Abbas, A., and Labbe-Bois, R. (1993) *J. Biol. Chem. 268*, 8541−8546.
26. Cramer, S. P., Tench, O., Yocum, M., and George, G. N. (1988) *Nucl. Instrum. Methods Phys. Res. A266*, 586−591.
27. http://www-ssrl.slac.stanford.edu/exafspak.html.
28. George, G. N., Garrett, R. M., Prince, R. C., and Rajagopalan, K. V. (1996) *J. Am. Chem. Soc. 118*, 8588−8592.
29. Rehr, J. J., Mustre de Leon, J., Zabinsky, S. I., and Albers, R. C. (1991) *J. Am. Chem. Soc., 113*, 5135−5140.
30. Mustre de Leon, J., Rehr, J. J., Zabinsky, S. I., and Albers, R. C. (1991) *Phys. Rev. B44*, 4146−4156.
31. Stiefel, E. I., and George, G. N. (1900) *Bioinorganic Chemistry* (Bertini, I., Gray, H. B., Lippard, S. J., and Valentine, J., Eds.) pp 365−453, University Science Books, Mill Valley, CA.
32. Allen, F. H., and Kennard, O. (1993) *Chem. Des. Autom. News 1*, 31−37.
33. Stevens, E. D. (1981) *J. Am. Chem. Soc. 103*, 5087−5095.
34. Strange, R. W., Blackburn, N. J., Knowles, P. F., and Hasnain, S. S. (1987) *J. Am. Chem. Soc. 109*, 7157−7162.
35. Blackburn, N. J., Strange, R. W., McFadden, L. M., and Hasnain, S. S. (1987) *J. Am. Chem. Soc. 109*, 7162−7170.
36. Poiarkova, A. V., and Rehr, J. J. (1999) *Phys. Rev. B 59*, 948−957.
37. Gorun, S. M., Papaefthymiou, G. C., Frankel, R. B., and Lippard, S. J. (1987) *J. Am. Chem. Soc. 109*, 4244−4255.
38. Liu, H. I., Sono, M., Kadkhodayan, S., Hager, L. P., Hedman, B., Hodgson, K. O., and Dawson, J. H. (1995) *J. Biol. Chem. 270*, 10544−10550.
39. Boyington, J. C., Gaffney, B. J., and Amzel, L. M. (1993) *Science 260*, 1482−1486.
40. Minor, W., Steczko, J., Stec, B., Otwinowski, Z., Bolin, J. T., Walter, R., and Axelrod, B. (1996) *Biochemistry 35*, 10687−10701.
41. Stoddard, B. L., Howell, P. L., Ringe, D., and Petsko, G. A. (1990) *Biochemistry 29*, 8885−8893.
42. Bond, C. J., Huang, J., Hajduk, R., Flick, K. E., Heath, P. J., and Stoddard, B. L. (2000) *Acta Crystallogr., Sect. D 56*, 1359−1366.
43. Roach, P. L., Clifton, I. J., Hensgens, C. M., Shibata, N., Schofield, C. J., Hajdu, J., and Baldwin, J. E. (1997) *Nature 387*, 827−830.
44. Adriat, A., Jacquamet, L., Le Pape, L., Gonzales de Peredo, A., Aberdam, D., Hazemann, J.-L., Latour, J.-M., and Michaud-Soret, I. (1999) *Biochemistry 38*, 6248−6260.
45. Alberts, I. L., Nadassy, K., and Wodak, S. J. (1998) *Protein Sci. 7*, 1700−1716.

BI015814M